*remote sensing*

MDPI

*Article*

# Simulation of BepiColombo's Gravity Investigation with Dynamical Mismodeling

**Ariele Zurria [1,*], Ivan di Stefano [1], Paolo Cappuccio [2], Umberto De Filippis [2] and Luciano Iess [1]**

[1] Department of Mechanical and Aerospace Engineering, Sapienza University of Rome, Via Eudossiana 18, 00185 Rome, Italy; ivan.distefano@uniroma1.it (I.d.S.); luciano.iess@uniroma1.it (L.I.)
[2] Aurora Technology for ESAC, Camino Bajo del Castillo s/n, 28692 Villanueva de la Cañada, Spain; paolo.cappuccio@ext.esa.int (P.C.); umberto.defilippis@ext.esa.int (U.D.F.)
* Correspondence: ariele.zurria@uniroma1.it; Tel.: +39-3485931117

## Highlights

**What are the main findings?**

- MORE can improve estimates of Mercury's gravity and rotation, even in the presence of dynamical modeling errors.
- A precise trajectory reconstruction cannot be achieved if three or more wheel off-loading maneuvers per day are scheduled.

**What are the implications of the main findings?**

- MORE is expected to provide a reliable, high-resolution gravity field in the southern hemisphere, complementary to MESSENGER's results in the northern polar region.
- Laser altimetry and geodetic control network will be adversely affected by the poor orbital reconstruction if three or more wheel off-loading maneuvers are operated daily.

## Abstract

The BepiColombo spacecraft, designed by ESA and JAXA, is currently in its cruise phase toward Mercury. Among the scientific investigations is the Mercury Orbiter Radio-science Experiment (MORE), which will exploit a multi-frequency microwave tracking system with an advanced Ka-band transponder to achieve its objectives pertaining to Mercury's geodesy and fundamental physics. Leveraging precise measurements from this state-of-the-art radio tracking system, MORE is expected to provide new insights into Mercury's interior, refining and expanding upon the findings of the MESSENGER mission. This work evaluates the performance of MORE's gravity and rotation experiment, specifically assessing how BepiColombo's improved radio tracking data can reduce uncertainties in the determination of Mercury's gravity field, Love number $k_2$, and rotational state. Differently from previous covariance analyses, this work includes errors in the dynamical model to assess the experiment's performance under controlled mismodeling conditions. We present the results of a numerical simulation covering BepiColombo's extended two-year orbital phase, with scientific operations set to begin in 2027.

**Keywords:** orbit determination; mercury; gravity field; bepicolombo; radio science

Check for updates

Academic Editor: Jianguo Yan

Received: 6 March 2026
Revised: 29 May 2026
Accepted: 3 June 2026
Published: 7 July 2026

**Copyright:** © 2026 by the authors. Licensee MDPI, Basel, Switzerland. This article is an open access article distributed under the terms and conditions of the Creative Commons Attribution (CC BY) license.

## 1. Introduction

Investigating Mercury is essential for improving our understanding of the early evolution of the inner Solar System and gaining insights into the formation of the Earth. However,

the planet's extreme environment, characterized by high radiation levels, intense heat and the significant energy required for orbital insertion, has made missions to Mercury particularly challenging. As a result, only two spacecraft have visited the planet so far: Mariner 10, which performed flybys in the 1970s [1], and MESSENGER [2], which became the first spacecraft to orbit Mercury. Despite their contributions, many fundamental questions remain unanswered, necessitating further investigation. To go beyond the achievements of these two past missions, the dual spacecraft BepiColombo was launched in October 2018 and is currently en route to Mercury. The spacecraft is composed of two orbiters: the Mercury Magnetospheric Orbiter (MMO), developed by JAXA, and the Mercury Planetary Orbiter (MPO), provided by ESA. Both orbiters will enter their final polar orbits around Mercury in late 2026 to conduct an extensive investigation of the planet [3–5]. The MPO carries a suite of eleven scientific instruments, including the Mercury Orbiter Radio-science Experiment (MORE), which is dedicated to geodesy and geophysics [6]. In addition, MORE will test gravitational theories during superior solar conjunctions (SSC) in the cruise phase [7], as well as in the orbital phase.

MORE relies on an advanced fully digital Ka-band transponder (KaT), designed to receive a Ka-band radio signal from Earth and retransmit it coherently in phase. The KaT operates in synergy with the Deep Space Transponder (DST), also onboard the MPO, which provides two-way coherent radio links at X/X and X/Ka bands. This multi-frequency link configuration allows the near-complete removal of noise due to solar plasma at almost all solar elongation angles [8]. The KaT also enables range measurements in Ka-band using a 24 megachips per second (Mcps) pseudo-noise (PN) modulation, which represents a custom implementation outside the commonly adopted specifications [9]. By leveraging this novel tracking technology for deep-space navigation, the MORE investigation is expected to drive new discoveries in space geodesy and to estimate parameters of relativistic gravity with unprecedented accuracy.

This paper aims to evaluate the performance of the gravity and rotation experiment conducted by MORE during BepiColombo's orbital phase, which can be decoupled from the relativity test [10]. For a detailed overview on the fundamental physics test, see [10,11]. During the real mission operations, data coming from the ISA accelerometer will be included in the orbit determination code to avoid significant mismodeling due to the strong and difficult-to-model non-gravitational accelerations. However, thermal drifts and other systematic effects affecting the accelerometer's measurements could introduce errors in reconstructing the spacecraft trajectory. To compensate for these issues, a dedicated calibration strategy is required. Other works have investigated the impact of accelerometer readout errors and calibration [10,12], showing that adding the accelerometer bias and bias rate in the fit degrades the uncertainties in rotational parameters, the Love number $k_2$, and low-degree gravity coefficients by a factor of two to three. However, considering the accuracy declared after ground tests [13], the use of accelerometer data would be very important to reduce errors on the orbital solution coming from dynamical mismodeling. Furthermore, the tool would become fundamental for the detection of unexpected accelerations that could degrade the orbital reconstruction [14,15].

In this work, we present a contingency analysis which relies on a comprehensive prediction of non-gravitational accelerations that are achievable through accurate numerical models, without ISA accelerometer measurements. Unlike previous analyses, this study incorporates various sources of mismodeling to simulate a perturbed dynamical state of the probe. These include errors in the spacecraft reference state and optical properties, unbalanced $\Delta$Vs due to wheel off-loading maneuvers, solar irradiance fluctuations, residual effects due to unmodeled non-gravitational accelerations and inaccuracies in the gravity

and rotation model of Mercury. The simulations are based on the latest mission scenario, with the science operations of the orbital phase beginning in April 2027.

The paper is organized as follows: an overview of the MORE gravity investigation is provided in Section 2; the methods adopted for the numerical simulations are reported in Section 3; the results are presented in Section 4; and finally, the concluding remarks are given in Section 5.

## 2. The MORE Gravity Investigation

MORE aims to conduct accurate measurements of the Hermean gravity to enhance our understanding of Mercury's interior structure. The onboard radio tracking system enables a highly accurate analysis of the spacecraft orbital motion, allowing for the retrieval of the static and time-varying gravity field of Mercury. The geodesy and geophysics experiment of MORE mainly focuses on the following areas:

- The determination of the static gravity field to about degree and order 40.
- The estimation of the Love number $k_2$ to investigate tidal variations in the gravity field.
- The characterization of Mercury's rotational state (pole direction and librations in longitude).

The improved estimates from MORE will provide key insights into Mercury's core structure. The unexpectedly large mean density of the planet (5427 kg/m$^3$, significantly larger than expected for its radius) and the measured magnetic field suggest that Mercury's core consists of a solid inner core and a conductive molten outer core, primarily composed of iron alloyed with lighter elements [16]. To verify this hypothesis, it is important to obtain information about the ratio between the principal moment of inertia of the mantle and that of the entire planet, represented as $C_m/C$. Estimating the pole's right ascension and declination allows us to determine the obliquity of the pole. The combination with the gravity quadrupole coefficient provides insights into the normalized moment of inertia $C/MR^2$, also known as the concentration factor. For a homogeneous body, this factor is expected to be 0.4, but for Mercury, it is anticipated to be lower. Following the Peale's procedure, we assume that the core does not experience the 88-day physical libration of the mantle but instead follows the mantle over the timescale of the 300,000-year precession of the spin in Cassini state 1 [17,18]. By estimating the physical librations in longitude, the concentration factor, and the degree 2 gravity field, we can obtain the ratio $C_m/C$. This ratio equals one for a rigid body and approximately 0.5 for a body with a liquid layer or core.

A comprehensive understanding of Mercury's interior relies on a thorough investigation on gravitational and deformation tides. MORE will enhance the characterization of Mercury's tidal response through measurements of the planetary gravity field from a low-eccentric orbit. The precise determination of the spacecraft orbit using MORE radio tracking data and ISA observations will improve the determination of $k_2$ and provide an initial estimate of its phase lag. These measurements will help constrain the rheological properties of the mantle and outer core. The measurement of Love number $h_2$, which measures the physical displacement of the planetary surface, will be obtained thanks to the onboard BepiColombo laser-altimeter (BELA) data processed with the accurate orbit products coming from MORE [19]. A combined knowledge of $k_2$ and $h_2$ will result in outstanding refinements of the interior modeling [20] and composition [21]. The determination of the lag angle and its uncertainty also holds significance as it provides an upper bound to the value of the quality factor Q of Mercury's mantle [6]. By jointly analyzing moments of inertia and Love numbers, we can obtain comprehensive geophysical constraints that facilitate a better understanding of Mercury's composition, size, and interior structure. These constraints are essential for refining interior modeling solutions and improving our knowledge of the planet [22].

The gravimetry experiment of MORE will provide accurate measurements of the gravity anomalies, which are due to the uneven distribution of mass in the planet. BELA will accurately map the topographic reliefs on the planetary surface, allowing for the computation of the Bouguer gravity anomaly, which consists of the difference between the measured gravity anomaly and the gravity predicted from topography [23]. The measured Bouguer anomalies play a fundamental role in investigating the structure of the crust and the upper mantle and in characterizing features in the deeper mantle, providing the possibility to study the thermal history of Mercury [24].

Updated versions of the Hermean gravity field obtained by processing MESSENGER radio science data have been published during the duration of the mission [25–27]. The orbit of MESSENGER was highly eccentric, with the pericenter located at ∼60°N. Because of the large altitude variations and the consequent uneven coverage of Mercury's surface, the normal equations of the batch-least square method used to analyze the MESSENGER radio tracking data required the use of a priori information to enable a smooth inversion of the problem. Usually, the a priori uncertainty on the gravity harmonic coefficients is constrained through the empirical Kaula rule [28]. The first global solution based on the complete dataset was HgM007 [29], estimated up to degree and order 100 (corresponding to a spatial resolution of ~80 km), with a Kaula constraint of $A_k$ = 3 applied beyond degree 10. This was later refined into the HgM008 model [16], maintaining the 100 × 100 resolution but adopting a slightly higher Kaula factor of $A_k$ = 4. Two different solutions up to degree and order 160, named MESS160A [30] and HgM009 [31], have been later retrieved through a reprocessing of the entire MESSENGER radio science dataset. The first one adopts a Kaula rule with $A_k$ = 5 and also discusses alternative constraint methods using surface acceleration measurements or the harmonic spectrum of gravity derived from topography. The second one is instead retrieved with a looser Kaula constraint ($A_k$ = 10), which led to an improved correlation with topography. These solutions achieved resolutions beyond degree 100 in the northern hemisphere (spatial scales better than 80 km). However, coverage over the equator and southern hemisphere remained limited, with resolutions near degree 15, corresponding to spatial scales of about 500 km.

As shown in previous analyses [12], MORE can complement MESSENGER coverage by resolving the gravity field up to about degree 40 in the southern hemisphere (spatial resolution of ~180 km), without assuming any regularization. The enhanced performance in the southern hemisphere results from the drift of the spacecraft pericenter, which progressively moves toward the south pole while decreasing in altitude due to perturbations from gravitational harmonics [32]. The complementary spatial coverage of the two missions offers a unique opportunity to achieve a high resolution gravity field at all latitudes, maintaining the fine-scale resolution at the northern hemisphere while significantly improving the recovery in southern latitudes.

## 3. Methods

The methodology behind this work consists of an orbit determination (OD) process [33], implemented through the Jet Propulsion Laboratory's MONTE OD code (version 164.1; [34]). This procedure can be decomposed in two main steps. The first step is the generation of synthetic observed observables by integrating the spacecraft trajectory, using a dynamical and observation model that we assume as the truth. White Gaussian noise consistent with the expected data accuracy is then added to these measurements. The second step is the least-squares estimation, where the simulated radio observables at the ground stations are compared with predictions computed using a best-guess reference model. The result of this comparison is a vector of observation residuals $\boldsymbol{y}$ (observed observables minus computed observables). A cost function, defined upon this vector, is

minimized by iteratively correcting the parameters of the reference model, collected in a state vector. At each iteration, the estimated values of the solved-for parameters and a covariance matrix are retrieved. The latter provides the associated formal uncertainties of the estimated parameters. The weighted least-squares differential correction $\hat{\boldsymbol{x}}_k$ to the state vector at iteration $k$ can be expressed as follows:

$$\hat{\boldsymbol{x}}_k = \left(\boldsymbol{H}_k^T \boldsymbol{W} \boldsymbol{H}_k + \overline{\boldsymbol{W}}_k\right)^{-1} \left(\boldsymbol{H}_k^T \boldsymbol{W} \boldsymbol{y}_k + \overline{\boldsymbol{W}}_k \bar{\boldsymbol{x}}_k\right) \tag{1}$$

where the matrix $\boldsymbol{H_k}$ contains the partial derivatives of the observable quantities with respect to the solve-for parameters and $\boldsymbol{W}$ is the matrix which contains the weights on the observables. The quantities $\bar{\boldsymbol{x}}_k$ and $\overline{\boldsymbol{W}}_k = \overline{\boldsymbol{P}}_0^{-1}$ represent the a priori state deviation vector and the inverse of the corresponding covariance matrix, respectively. The quantity $\boldsymbol{P_k} = \left(\boldsymbol{H}_k^T \boldsymbol{W} \boldsymbol{H_k} + \overline{\boldsymbol{W}}_k\right)^{-1}$ is the covariance matrix of the estimated state deviation vector.

We introduce discrepancies between the dynamical model used for the generation of synthetic radio-observables and the one used in the estimation process (see Section 3.4). This means that the computed observables are obtained from a reconstructed trajectory, which differs from the "true" trajectory used to generate the synthetic dataset. Differently from covariance analyses, this procedure allows an assessment of the OD performance in the presence of modeling errors.

### *3.1. Constrained Multi-Arc Approach*

The multi-arc strategy is employed to reduce the effects of unmodeled accelerations by introducing an over-parameterization of the problem [35]. This approach divides the spacecraft trajectory into distinct, non-overlapping arcs, each treated independently with their own estimated set of initial conditions. By handling each arc separately, errors that accumulate over time due to dynamical mismodeling can be minimized. However, this comes at the expense of discontinuities in the estimated trajectory at the transition points between arcs.

In a multi-arc approach, the solve-for parameters are divided into locals and globals. Local parameters, such as the spacecraft state vector and velocity increments from maneuvers, are estimated independently within each arc. In contrast, global parameters, like the harmonic coefficients of the gravity field, remain constant across all arcs and throughout the entire mission. The observation model is structured accordingly, with the matrix $\boldsymbol{H_k}$ explicitly distinguishing between the contributions of local and global parameters to the observed quantities.

Since there is no correlation between parameters belonging to different arcs, trajectory discontinuities naturally arise at the transition points between arcs. To address this, a constrained multi-arc approach can be applied, where the differences in position and velocity between consecutive arcs are constrained within predefined thresholds [36]. The optimal constraint values are determined through a trade-off between maintaining solution stability and ensuring that the constraints effectively reduce discontinuities.

### *3.2. Observable Quantities*

The observables produced by MORE consist of range and Doppler (range-rate) measurements, obtained by establishing microwave radio links between the spacecraft and ground stations [37]. The range rate is derived from the Doppler shift in an electromagnetic wave transmitted from the ground, received by the spacecraft, and coherently retransmitted back to Earth in a two-way coherent configuration. The spacecraft range is obtained by measuring the time interval between the transmission and reception of a known signal modulated onto the carrier.

Since the focus of this analysis is the gravity experiment, which is largely decoupled from the relativity tests and the associated update of Solar System ephemerides, we opt for a more conservative and robust approach by excluding range data. Dedicated analyses have shown that the contribution of range data to the recovery of Mercury's gravity field and rotational state is comparatively limited, mainly improving the estimation of the low-degree gravity coefficients and rotational parameters at the level of 10–20% at most.

We simulate data acquired at elevation angles above 15° to prevent degradation caused by tropospheric effects. The primary observables are range-rate in Ka-band, established with the DSA-3 ground station of ESA's ESTRACK network, located in Malargüe (Argentina). This station will serve as the primary ground facility for tracking, telemetry, and command (TTC) operations and is the only ESTRACK station with Ka-band uplink capabilities. Additionally, we account for a switch to the DSA-2 ground station in Cebreros (Spain), which will provide X-band tracking during June 2027 due to data volume constraints. Preliminary inflight performances of the Ka-band two-way Doppler were in good agreement with the predictions made in the design phase of the radio science experiment (0.024 mm/s @ 30 s; [38]). The degradation of the radiometric accuracy is mainly driven by plasma-induced dispersive effects when the radio signal propagates close to the Sun. However, recent analyses have demonstrated that radiometric data acquired at small Sun–Probe–Earth (SPE) angles can still be exploited within the OD process [39,40]. We conservatively excluded all the radiometric observables acquired with an impact parameter $\boldsymbol{b}$ (defined as the shortest distance between the center of the Sun and the line of sight) within 7 solar radii, where noise levels may significantly deviate from the assumptions of this work. Before and after each perihelion, when Mercury's true anomaly (MTA) is $\pm 40°$, the Ka-band transponder is expected to be switched off due to power limitations, leaving only X-band tracking available. Table 1 shows the observable types and noise levels assumptions, which are based on preliminary considerations from [40]. All the observables are sampled at an integration time of 30 s. About 9% of the observables are filtered to account for occultations by Mercury and about 25% for outages of the High Gain Antennas (HGA), which occur when the HGA is blocked by other parts of the spacecraft.

**Table 1.** Observable types and noise level assumptions.

| Scenario | Station | Measurement Type | Noise Level @ 30 s [$\mu$/s] |
|---|---|---|---|
| $MTA > 40°$, $\boldsymbol{b} > 7\ R_\odot$ | DSA-3 | Two-way Ka-band range-rate | 24 |
| $MTA \leq 40°$, $\boldsymbol{b} > 30\ R_\odot$ | DSA-3 | Two-way X-band range-rate | 87 |
| $MTA \leq 40°$, $7\ R_\odot < \boldsymbol{b} \leq 30\ R_\odot$ | DSA-3 | Two-way X-band range-rate | ~1000 |
| Switch to Cebreros (June 2027) | DSA-2 | Two-way X-band range-rate | 87 |

### *3.3. Dynamical Model*

Our dynamical model accounts for the gravitational monopole accelerations due to Solar System planets, the spherical harmonics coefficients of the Sun up to degree and order 2 and the spherical harmonics coefficients of Mercury, provided by the MESSENGER mission. The field is truncated at degree and order 100, although the sensitivity is well below those harmonics because of the orbital altitude of the MPO, which stays above 200 km at the pericenter during the entire mission. The gravity field coefficients are defined in the body-fixed frame of the surface. The orientation of Mercury is given by the International Astronomical Union's (IAU) standard [41], which for Mercury includes pole direction, precession and librations in longitude.

Due to the proximity between the spacecraft and the Sun, BepiColombo will experience significant non-gravitational accelerations. These accelerations originate from different sources: direct sunlight (solar radiation pressure), sunlight reflected by the planet (albedo

pressure), infrared radiation emitted by the planet (thermal infrared pressure) and by the spacecraft (thermal recoil pressure). Figure 1 shows the magnitude of each component of the modeled non-gravitational accelerations for the nominal mission, which spans a one-year orbital phase.




**Figure 1.** Non-gravitational accelerations module during the nominal mission. The plot shows the contributions from solar radiation pressure (SRP), planetary radiation pressure (albedo + infrared), and thermal recoil pressure (TRP). The sharp acceleration drops caused by geometric conditions appear as filled segments due to the plot's scale. The SRP double-peak structure within the orbital cycle is due to the commanded spacecraft attitude, which is reversed through flip-over maneuvers every half of the Mercury orbital period.

To model the effect of non-gravitational accelerations, a detailed representation of the spacecraft shape is required. In this analysis, the spacecraft is represented as a set of plates: the bus consists of six plates, while the solar array is modeled as a plate with a surface area of 8 $m^2$. The HGA is approximated as a parabola with a radius of 0.55 m and a depth of 0.47 m. Secondary surfaces, such as the two extendable booms, are not considered, as their contribution to the overall acceleration is negligible. The thermo-optical coefficients of the surfaces in the visible and infrared wavelengths have been provided by the spacecraft prime contractor AIRBUS (Blagnac, France). The effective area exposed to solar and planetary radiation is determined by the orientation of the spacecraft bus and solar panel, which is reproduced from preliminary specifications supplied by ESA. The spacecraft body fixed reference frame is oriented such that the +Z axis is nadir-pointing. The +X axis is aligned with the along-track direction for half of the Mercury orbit and is reversed through flip-over maneuvers during the other half. The normal for the solar array cells is tilted by 66°, with respect to the +Y axis of the spacecraft frame. Although the actual non-gravitational accelerations experienced during the orbital phase may differ from the predicted values due to potential deviations in the spacecraft real attitude, this discrepancy is not the primary focus of this study. Instead, the objective is to assess the impact of inconsistencies between the acceleration models used to simulate the tracking data and those adopted during the parameter estimation phase, as detailed in the following section.

The dominant non-gravitational force acting on the MPO is due to solar radiation pressure (SRP), whose intensity increases as the spacecraft gets closer to the Sun. The total SRP acceleration is determined by summing the individual contributions from all spacecraft sunlit surface elements. In the plot, the SRP acceleration is shown as a cyan line. During solar eclipses, SRP drops sharply to zero, creating discontinuities. Due to the plot's scale and resolution, these drops appear as filled segments along the curve.

The next most significant effects are due to the accelerations induced by planetary albedo (ALB) and infrared radiation (IR), shown as a green line. The albedo map, shown in Figure 2, is derived from the MESSENGER Mercury Dual Imaging System (MDIS; [42]) low-incidence angle (LOI) global map, which reveals the varying reflectance properties of Mercury's surface. The thermal infrared emissivity is obtained from a temperature map, also shown in Figure 2. This map is generated by discretizing Mercury's surface into a $1^\circ \times 1^\circ$ grid in longitude and latitude. At each grid point, the temperature is determined with a simple heat balance equation under the assumption of thermal equilibrium, considering the incoming solar radiation. Spatial and temporal temperature variations on the nightside are neglected, and a uniform temperature (100 K; [43]) is assumed for shadowed regions. While this approach captures the first-order thermal behavior, more sophisticated thermophysical models can be adopted for the future data analysis. The resulting albedo and emissivity distributions are then expanded into spherical harmonics using the SHTOOLS open-source library [44], as required by the MONTE software. To calculate the albedo and IR, the OD code discretizes the visible portion of Mercury's surface using a central cap and concentric rings. The total effect is computed by summing the contributions from all spacecraft surfaces exposed to the planet. These accelerations exhibit a sharp peak when the spacecraft passes over the sunlit region and drop rapidly afterwards in the night side. The albedo acceleration arises only from solar radiation reflected by Mercury's sunlit regions and drops to zero when the spacecraft is in the planet's shadow. In contrast, the thermal infrared acceleration also accounts for Mercury's night-side surface temperature, reaching a minimum in shadow but remaining non-zero.

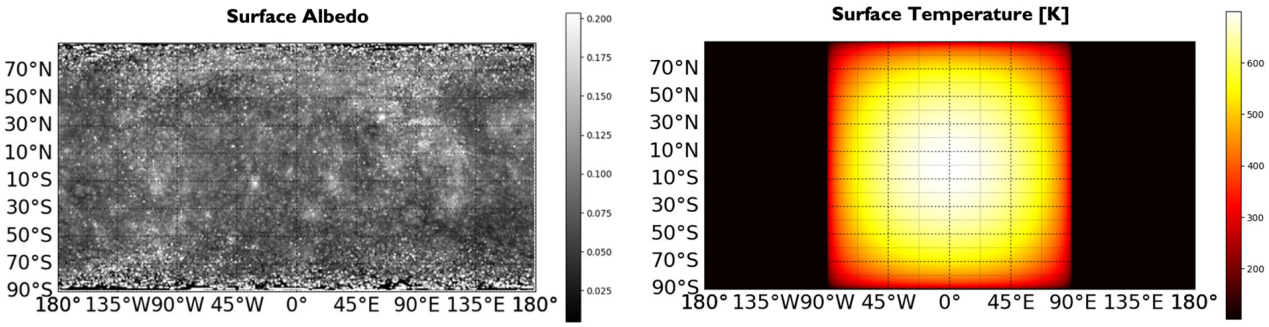



**Figure 2.** Albedo (**left**) and temperature (**right**) maps of Mercury. The albedo map is derived from the MDIS LOI map [42]. The temperature map is calculated in a reference frame with the X axis coincident with the position direction of the Sun, relative to Mercury.

Thermal recoil pressure (TRP), shown in Figure 1 as a red line, primarily arises from the anisotropic re-emission of absorbed solar radiation by the spacecraft external surfaces. For planetary orbiters, albedo and thermal infrared emission from the planet can contribute significantly to the net radiation on the spacecraft. This effect is particularly pronounced in the harsh thermal environment of Mercury, where TRP magnitude is up to ~20–25% of the SRP [45,46]. Each spacecraft plate is assigned an emissivity value, thermal capacity, surface area, and normal vector. The temperature of each plate is then determined by solving the differential heat balance equation, accounting for energy inputs from both the

Sun and Mercury. The resulting acceleration is obtained by summing the contributions of all spacecraft surfaces to the infrared emission.

The presence of a single solar panel and the asymmetric shape of the spacecraft generate large torques. Reaction wheels are used to counteract these effects and maintain the spacecraft attitude. While the original mission plan foresaw one wheel off-loading maneuver per day to dump excess angular momentum, this was later updated to two maneuvers per day: the first one occurred at apoherm during the tracking pass and the other after the pass, with a time interval of ~12 h between them. This operational configuration is adopted as the nominal scenario in our analysis. However, due to an unexpected performance issue with the reaction wheels close to zero angular velocity, mission planners are also evaluating alternative configurations that involve different wheel off-loading strategies. The increased frequency of the desaturation events will adversely affect the trajectory reconstruction. An alternative scenario with one maneuver every three orbits at apoherm (3 or 4 maneuvers per day) is discussed later. The residual ΔVs due to thruster's misalignment are included in the dynamical model to account for their impact on the spacecraft motion.

### *3.4. Dynamical Mismodeling*

The inaccurate modeling of the non-gravitational accelerations generates errors in the orbit determination and biases in scientific measurements that may lead to incorrect conclusions. To simulate a realistic operational context, we deliberately introduce mismatches between the force models employed for generating synthetic radio tracking data and those used during the OD process. Figure 3 shows the pre-fit errors on the predicted non-gravitational accelerations during the nominal mission. Consequently, the numerical integration of the spacecraft equations of motion during the estimation step yields a trajectory that deviates from the simulated "true" path, with the divergence increasing over time. Before the first filter correction, trajectory errors reach approximately 2–3 km in total position, with the largest contribution occurring in the transverse direction.

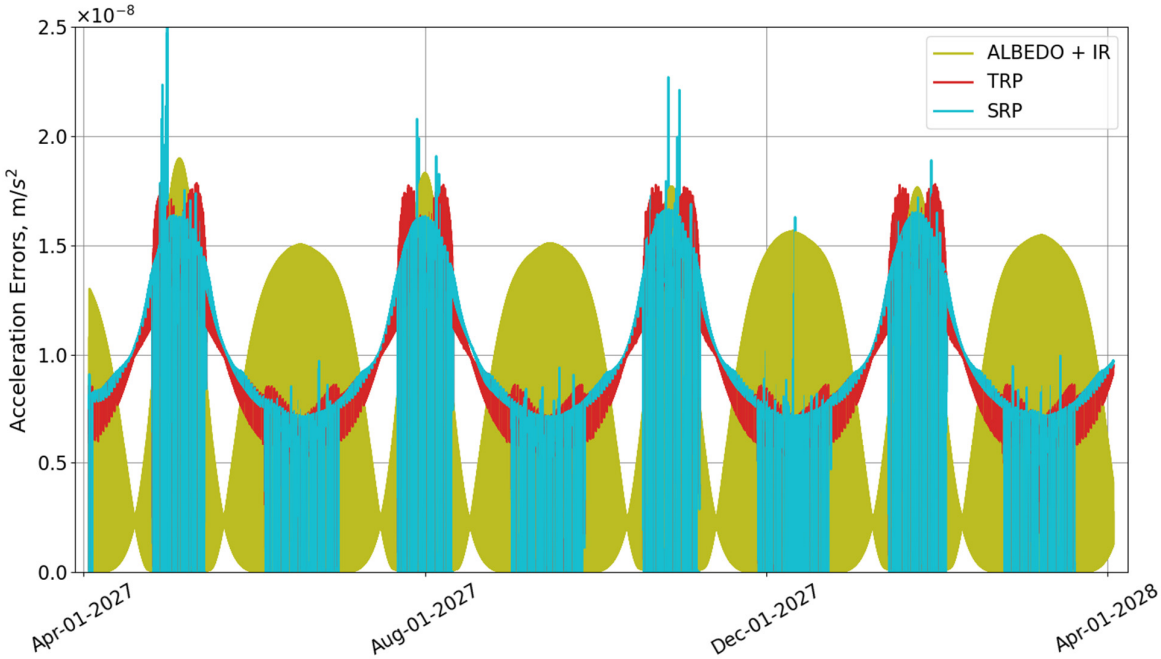



**Figure 3.** Module of non-gravitational acceleration pre-fit errors during the nominal mission. The plot shows the contributions from solar radiation pressure (SRP), planetary radiation pressure (albedo + infrared), and thermal recoil pressure (TRP).

It is important to note that there are some limitations in this approach. First, we are using the same software for synthetic data generation and parameter estimation. This means that, while we introduce mismatches between the force models, both rely on the same numerical algorithms. In addition, the models do not include secondary effects such as sporadic unexpected accelerations (e.g., due to gas leaks), which may locally degrade the orbit reconstruction. However, as discussed later, not every source of perturbation included in the data simulation model is associated with dedicated solve-for parameters adjusted during estimation. As a result, the estimation model attempts to reconstruct the spacecraft trajectory using a parameterization that differs from the one used to generate the synthetic observables, leaving part of the mismodeling intentionally unabsorbed. This methodology allows us to evaluate the stability of the orbital solution and the reliability of the recovered geophysical parameters under controlled mismodeling conditions.

#### 3.4.1. Reference State

The initial position and velocity conditions used to integrate the spacecraft trajectory during the estimation process are intentionally perturbed with respect to the "true" state used to generate the synthetic observables. These random perturbations are obtained from a bounded uniform distribution. The perturbation limits are set to $\pm$[0.5 m, 100 m, 100 m] for the position components and $\pm$[6 cm/s, 8 mm/s, 6 cm/s] for the velocity component in the radial, transverse, and normal (RTN) frame. These values are derived from the formal uncertainties obtained from a pure covariance analysis, increased by a factor of 10.

#### 3.4.2. Wheel Off-Loading Maneuver

Wheel off-loading maneuvers introduce velocity increments, $\Delta Vs$, that affect the orbital motion. The expected magnitude of the $\Delta Vs$ is 17 mm/s, 0.2 mm/s and 42 mm/s in the RTN orbital reference frame [10]. According to the specifications from the spacecraft manufacturer, these velocity variations will be known with a 5% uncertainty [47]. We model residual maneuver errors by drawing random perturbations from a bounded uniform distribution with limits set to $\pm$10% of the nominal values.

#### 3.4.3. Thermo-Optical Properties

Ground-measured values of reflectivity, emissivity, and absorptivity deviate from their actual in-flight values and continue to degrade over time due to exposure to the space environment. In this study, the spacecraft shape model used for the generation of synthetic observables assumes the expected end-of-life values for each surface. In the dynamical model of the estimation step, we include errors equal to 20% of their predicted end-of-life values on both specular and diffuse coefficients of the exposed sides of the array and the bus. While variations in these coefficients may partially compensate for each other, reducing their combined effect, the corresponding residual acceleration mismodeling is at the level of $10^{-8}$ m·s$^{-2}$ for both solar and planetary radiation pressure acceleration.

#### 3.4.4. Albedo and Infrared Scale Factors

Beyond thermo-optical properties, the computation of non-gravitational accelerations due to planetary radiation is subject to several additional error sources, including simplifications in the surface temperature model, truncation effects in the spherical harmonic expansion of albedo and emissivity, and the discretization of the visible cap in concentric rings. We assume that, by the end of the orbital phase, temperature and albedo maps of Mercury will be available with sufficient accuracy to constrain the total mismodeling of albedo and IR accelerations to be at the level of $10^{-8}$ m·s$^{-2}$. To account for this effect, in the estimation process, we increase both the albedo and IR accelerations magnitude by 10%. For some elements of the spacecraft shape, this increment partially compensates for the

mismodeling introduced through errors in the thermo-optical coefficients, resulting in a maximum acceleration mismatch of ~$2 \times 10^{-8}$ m·s$^{-2}$.

#### 3.4.5. Thermal Recoil Pressure

The acceleration induced by thermal re-radiation from the spacecraft surfaces depends on their temperature distribution, which is influenced by variations in the emissivity, absorptivity, and heat capacity. The modeling of this acceleration is particularly challenging due to the difficulty in predicting the temperature of the spacecraft elements. The dynamical model used to simulate synthetic observables incorporates the TRP acceleration calculated with the predicted end-of-life values of the spacecraft thermo-optical properties. On the other hand, the acceleration in the estimation model is computed with the perturbed coefficients, but these coefficients are kept fixed and are not updated throughout the iterative procedure. These discrepancies propagate into residual acceleration errors of ~20% of the nominal thermal recoil pressure.

#### 3.4.6. Solar Irradiance Fluctuations

The value of the solar flux shows temporal random fluctuations ranging at the level of [0.01, 0.1]% of the central value over a few hours. These oscillations of the solar irradiance are due to the simultaneous effect of faculae and sunspots on the solar surface [48]. Space-based radiometers on board satellites in Earth's orbit can measure these irradiance fluctuations with excellent accuracy [49]. To generate the observed observables, we use a constant value for the solar flux, while the estimation model includes irradiance fluctuations extrapolated from past measurements of the SORCE mission (Figure 4). The data is sampled every 6 h and represents the value of Total Solar Irradiance (TSI) at 1 AU from the Sun, which is time-shifted by approximately two solar cycles to align it with the BepiColombo mission timeline. The faint signal induced by SRP fluctuations is up to $10^{-10}$ m·s$^{-2}$, well below the level induced by the other perturbations.

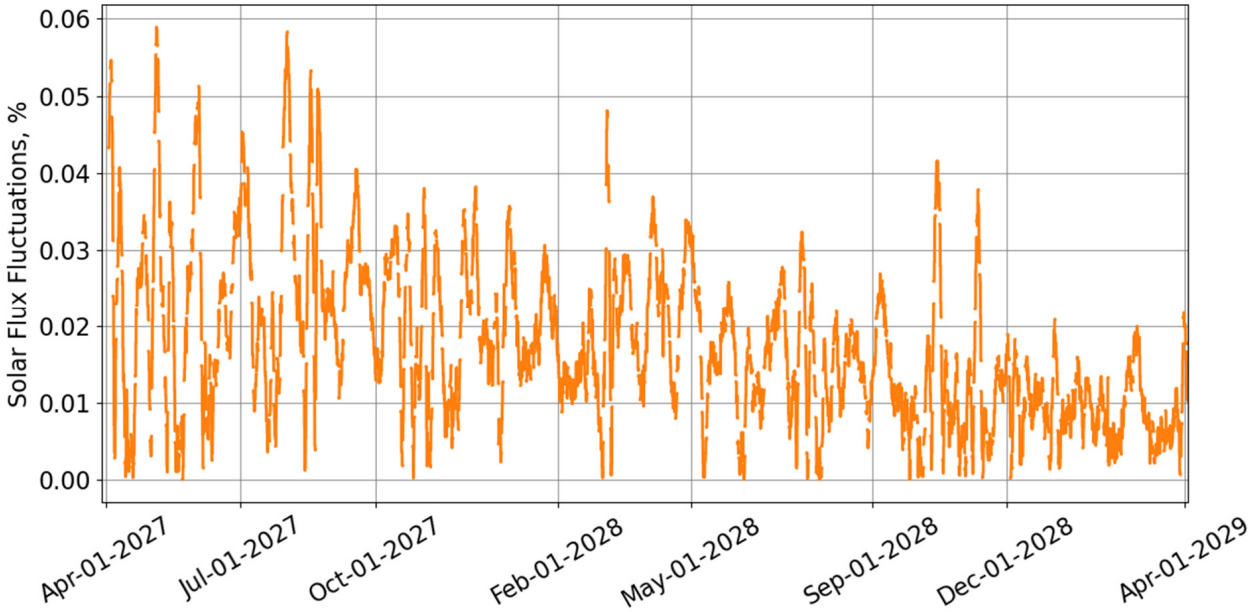



**Figure 4.** Fluctuations of solar flux from SORCE mission [49]. The dataset provides values of the Total Solar Irradiance (TSI) at 1 AU from the Sun, which are time-shifted by approximately two solar cycles to align them with the BepiColombo mission timeline and resampled at 6-hour intervals.

3.4.7. Gravity and Rotation

The Mercury gravity field used for trajectory integration is derived from the latest MESSENGER gravity solutions [30,31]. Due to the highly eccentric orbit of the spacecraft, MESSENGER gravity measurements provide good high-resolution coverage only for the northern hemisphere (the resolution and accuracy in the other hemisphere is much lower). Synthetic observables are generated using the HgM009 gravity field [31], while the estimation process is initialized with the MESS160A gravity coefficients [30]. Both solutions are truncated at degree and order 100. Figure 5 shows the spectral decomposition of the two gravity fields, calculated as follows:

$$C_l = \sqrt{\frac{1}{2l+1}\sum_{m=0}^{l}\left(\overline{C}_{lm}^2 + \overline{S}_{lm}^2\right)} \quad (2)$$

where $\overline{C}_{lm}$, $\overline{S}_{lm}$ are the normalized spherical harmonics coefficients. We also adopt the different gravitational constants and rotational parameters associated with each gravity solution. Table 2 summarizes the values used for Mercury's GM, real part of $k_2$, spin axis orientation, and angular velocity. The libration amplitude is fixed at 38.5 arcsec, corresponding to the central value estimated by [50].

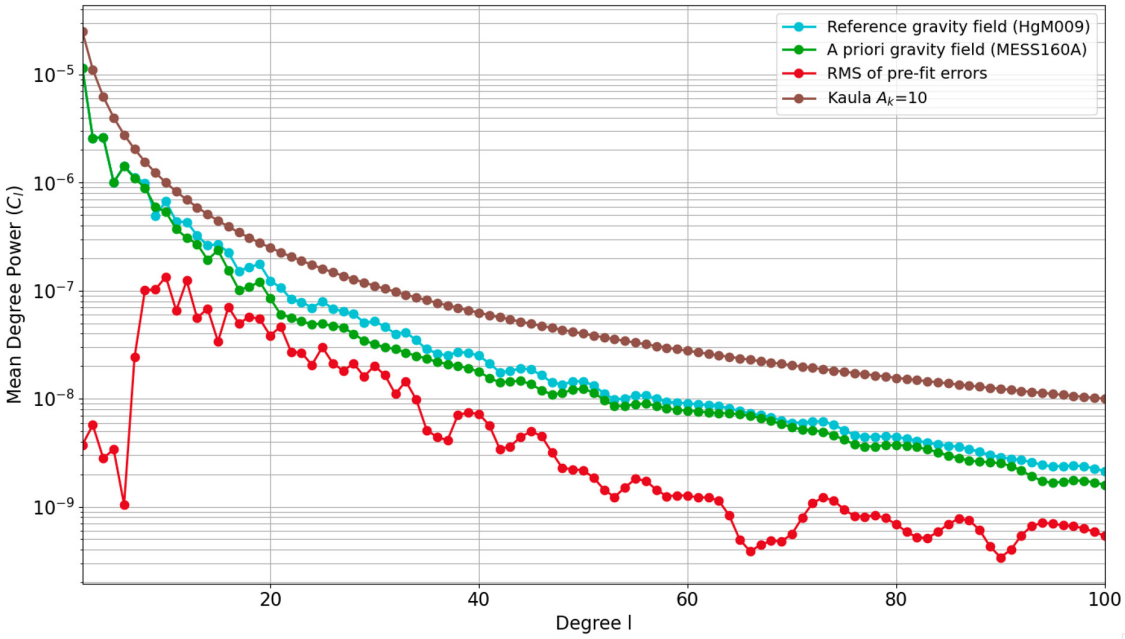



**Figure 5.** Spectral decomposition of the gravity fields used for data generation and for the estimation, with the corresponding difference between the two solutions and the Kaula power law with $A_k$ = 10.

**Table 2.** Values used in the generation of synthetic observables [16] and corresponding a priori values in the estimation model [30].

| Parameter | Dataset Generation | Estimation |
|---|---|---|
| Mercury GM [km$^3$/s$^2$] | 22,031.863566 | 22,031.868691 |
| $k_{2r}$ | 0.569 | 0.53 |
| Spin axis $\alpha$ [deg] | 281.0082 | 281.0138 |
| Spin axis $\beta$ [deg] | 61.4164 | 61.4161 |
| Mercury angular velocity $\omega$ [deg/day] | 6.1385054 | 6.1385140 |

### *3.5. Simulation Strategy*

We simulate the extended two-year orbital phase according to the current mission scenario, with the scientific operations beginning in April 2027. The division of the timespan in arcs is done by attributing to each arc a duration of 24 h to include a daily tracking window from DSA-3. For about 20 days, in June 2027, only X-band tracking is expected to be available from DSA-2. With this choice of arc length, the accumulated mismodeling errors are not expected to grow to a level that would prevent an adequate fit to the observations. The state vector is determined at the central time of each arc, integrating forward and backward. Figure 6 shows a typical arc configuration.

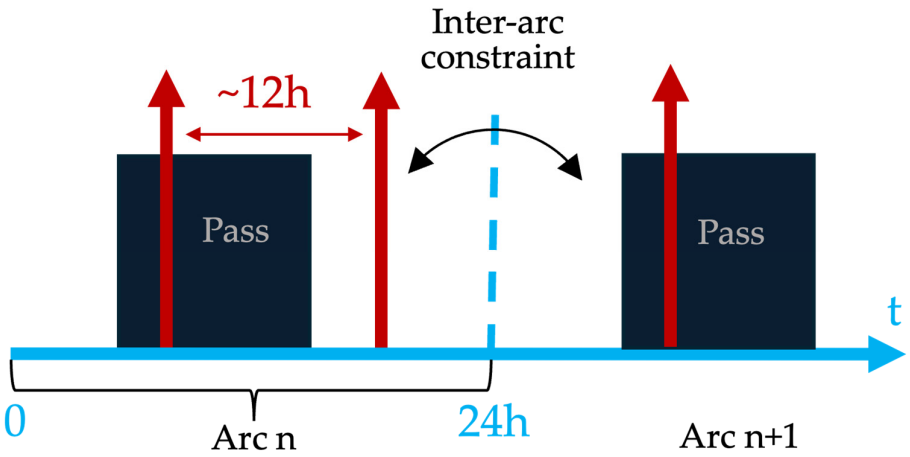



**Figure 6.** Arc configuration. Each arc includes a daily tracking window (blue square) and two wheel off-loading maneuvers (red arrows).

Tables 3 and 4 show the orbital parameters of the reference trajectory at the beginning of the scientific phase and the set of estimated parameters with their a priori uncertainties, respectively.

**Table 3.** Orbital parameters of the reference trajectory.

| **BepiColombo Reference Trajectory** | |
|---|---|
| Semi-major axis | 3430 km |
| Pericenter radius | 2905 km |
| Apocenter radius | 3955 km |
| Eccentricity | 0.153 |
| Inclination | 90 deg |
| Right ascension of the ascending node | 111 deg |
| Argument of pericenter | 13 deg |

The local parameters are the spacecraft state at the reference epoch of the arc and the uncompensated ΔVs related to the WOL maneuvers. The thermo-optical coefficients of the surfaces and scale factors for TRP are included in the local parameters to absorb mismodeling errors. We emphasize that, although we do not account for sporadic unexpected accelerations, several perturbations are intentionally incompletely represented by the set of solve-for parameters. For example, during the estimation process, the TRP acceleration is computed using perturbed thermo-optical coefficients, but these coefficients are kept fixed and are not updated throughout the iterative estimation procedure. Consequently, the residual mismodeling cannot be fully corrected and can only be partially absorbed by the estimated TRP scale factors. Similarly, the albedo and IR accelerations are affected simultaneously by errors in the thermo-optical properties and by variations in their associated scale factors. We intentionally do not include an albedo and thermal IR scale factor in the

set of solve-for parameters, forcing the estimation to absorb the mismodeling only through the thermo-optical coefficients. Finally, no scaling factor is estimated for the solar radiation pressure, despite the small solar irradiance fluctuations included in the simulation.

In a pure multi-arc strategy, trajectory discontinuities naturally arise at the transition points between arcs. These discontinuities are larger due to the presence of WOL maneuvers that occur outside the tracking passes. However, having a continuous, accurately reconstructed trajectory, without gaps induced by unmodeled maneuvers, would be highly desirable for the other instruments, especially the BELA laser altimeter [19]. For this reason, we include inter-arc constraints to reduce the discontinuities in phase space. The constraints enable the estimation of the out-of-pass maneuvers, which otherwise would be unobservable. If the values of the constraints are chosen properly, these continuity conditions generally lead to smaller formal uncertainties on position and velocity compared to an unconstrained multi-arc solution. However, the tightness of the constraints must be carefully adjusted, as it may introduce biases and compromise the robustness of the solution. In this analysis, we impose continuity constraints of 1 m in the J2000 reference frame. By multiplying this spatial tolerance by the mean motion ($7.3 \times 10^{-4}$ rad/s), we derive the corresponding velocity constraint (0.73 mm/s). The same values have also been used in [10] and reflect a balanced trade-off between the effectiveness of the constraint and the stability of the solution. Using tighter inter-arc constraints would force stronger continuity between adjacent arcs and would therefore produce more optimistic orbit reconstruction performances. At the current stage, however, such tight constraints cannot be properly justified or validated prior to the orbital phase and the availability of real tracking data. In Section 4, we discuss another scenario with no inter-arc constraints and one-maneuver every three orbits.

The estimated global parameters are shown in Table 4. Given that the geodesy and geophysics investigation is conceptually independent from the relativity experiment, we assume the framework of general relativity to be exact. We adopt the DE432 planetary ephemerides, an update of the DE430 solution [51], and no errors are applied to the state vectors of Mercury or the Earth at the reference epoch. This assumption is supported by the fact that our analysis is based exclusively on Doppler measurements, which exhibit minimal sensitivity to inaccuracies in planetary ephemerides. Refinement of planetary ephemerides can be performed separately by also using range data, in combination with the estimate of relativistic parameters [6].

**Table 4.** Set of estimated parameters and corresponding a priori uncertainties.

| **Local Parameter** | **A Priori Uncertainty** |
|---|---|
| S/C position (J2000) | 300 m |
| S/C velocity (J2000) | 10 cm/s |
| Uncompensated ΔVs (J2000) | [6.0, 4.0, 4.0] mm/s |
| Optical coefficients (visible and infrared) | 30% of the ref. value |
| TRP scale factors X, Y, Z (S/C frame) | 0.2 |
| **Global Parameter** | **A Priori Uncertainty** |
| Mercury $GM$ | Unconstrained |
| Gravity field coefficients $70 \times 70$ | $10^{-4}/l^2$ for $l > 30$ |
| Mercury $k_2$ | Unconstrained |
| Spin axis $\alpha$, $\delta$ | Unconstrained |
| Libration amplitude $\phi_0$ | Unconstrained |
| Mercury angular velocity $\omega$ | Unconstrained |

In contrast to previous studies that solved for the gravity field up to degree 50 without regularization, we extend the estimation to degree 70. This more conservative scheme is justified by the fact that gravity field coefficients were perturbed up to degree 100

in our simulations. Although estimating up to degree 50 is sufficient for the nominal phase, including higher-degree terms during the extended phase mitigates the risk of introducing biases, as the sensitivity to shorter-wavelength gravity signals increases due to the pericenter drift. To mitigate numerical instability, we apply a Kaula-type constraint starting from degree 31 onward [28]. Specifically, we use a Kaula factor $A_k = 10$, which is the value used in the reference gravity solution [31]. The choice of degree 30 as the transition point for regularization reflects the global resolution that is attainable by the experiment [10]. All the other estimated global parameters are unconstrained. To assess the sensitivity of the solution to the adopted regularization, we perform additional tests with a weaker or absent Kaula constraint. While the gravity field can still be satisfactorily reconstructed even with weaker constraints, the use of looser constraints substantially increases the formal uncertainties in the recovered gravity anomalies. For Mercury, expected Kaula factors are typically around 4–7 [31,52], and previously published gravity field solutions have generally used values equal to or smaller than 10 [16,26,30,31]. In this context, significantly weaker constraints would not be justified for Mercury's gravity spectrum.

## 4. Results

This section presents the expected performance of the gravity and rotation experiment, accounting for the dynamical modeling errors listed in Section 3.4. We also address the spacecraft orbit reconstruction performance, considering the occurrence of 2 WOL maneuvers per day. The impact of an increment of WOL events frequency is discussed.

### *4.1. Gravity*

A comparison of the power spectrum curves ($C_l$) of the estimated errors and uncertainty for the retrieved gravity is shown in Figure 7. The errors, calculated with respect to the gravity model used for synthetic data generation, remain within the 3-σ uncertainty envelope, indicating that the estimation process effectively compensates for dynamical mismodeling without introducing significant biases.

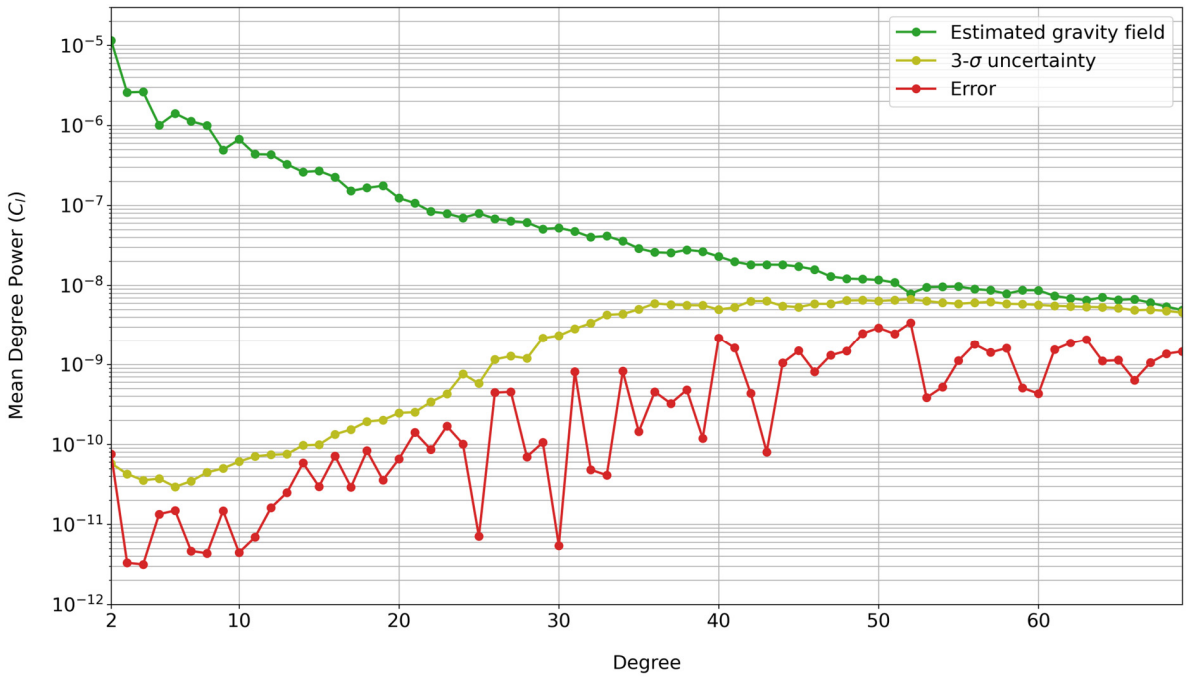



**Figure 7.** Spectral decomposition of the estimated gravity field, with the corresponding error and uncertainty spectrum.

In this analysis, we estimate up to degree 70, with a Kaula constraint ($A_k$ = 10) applied for degrees greater than 30. This scheme stabilizes the solution and entails conservative uncertainties. While it does not improve the intrinsic spatial resolution of the solution, we found that this approach enables a more robust recovery of the gravity field in the presence of dynamical mismodeling, whereas limiting the solution to degree 50 led to additional biases in the gravity coefficients.

As shown in Figure 8, the uncertainties in gravity anomalies over most of the southern hemisphere are at the level of ~10 mGal, indicating a promising opportunity for improved measurements of internal mass distributions and comparisons with surface topography. These uncertainties are larger, with respect to the ones shown in previous works [6], primarily due to the significant data loss caused by HGA outages and perihelia, and the estimation of higher-degree gravity coefficients under a relatively loose Kaula regularization. Approximately 99% of errors in the gravity anomalies, calculated with respect to the reference gravity model, are smaller than the 3-σ uncertainty, as shown in Figure 9.

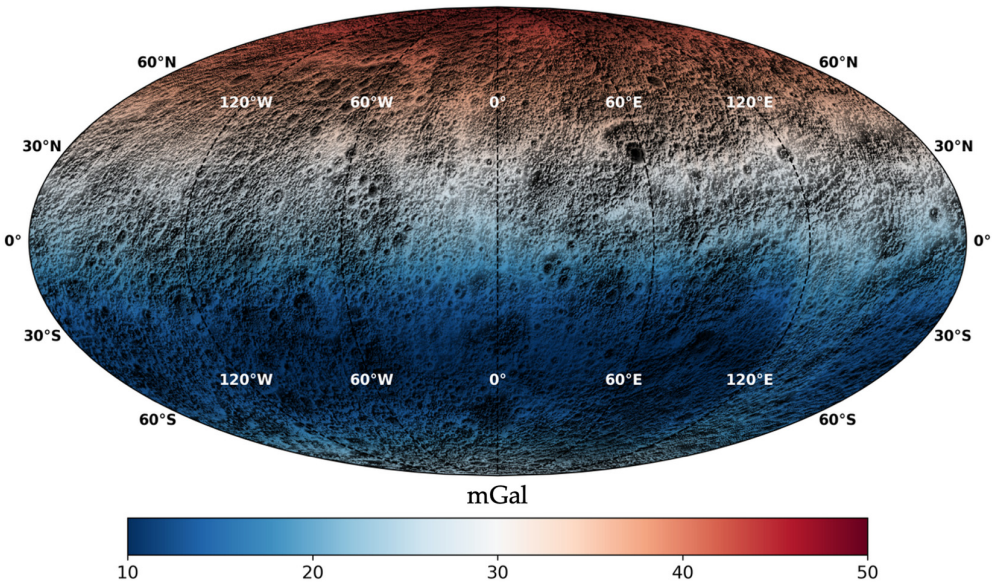



**Figure 8.** Mercury gravity anomalies 1-σ uncertainty.

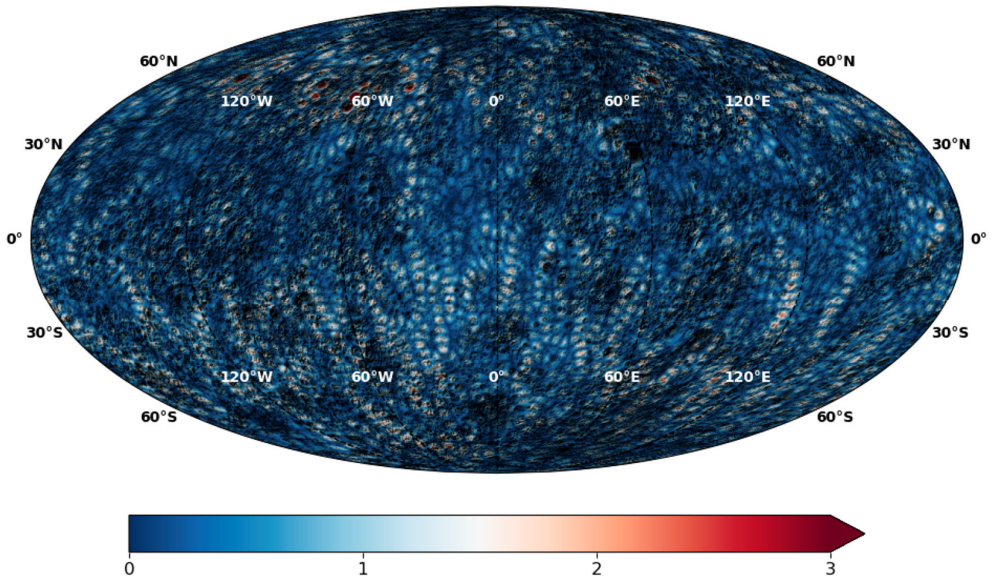



**Figure 9.** Mercury gravity anomalies error over 1-σ uncertainty.

Tables 5 and 6 present the error and accuracy attained by MORE in estimating the static degree 2 gravity coefficients and the tidal Love number $k_2$. All the reported 3-$\sigma$ uncertainties are compared with previous gravity solutions from MESSENGER [16,30]. The errors are below 3-$\sigma$, indicating that the estimated values are consistent with the ones used to simulate the radio tracking dataset. Furthermore, MORE will substantially improve the determination of these quantities with respect to the current knowledge. The real and imaginary part of the $k_2$, a crucial quantity for the geophysical models of Mercury's interior structure, can be determined with an uncertainty of $1.3 \times 10^{-3}$ and $1.2 \times 10^{-3}$, respectively. These refined estimates will strongly constrain Mercury's interior structure, the rheological properties of Mercury's mantle and the range of interior models compatible with rotational measurements [22].

**Table 5.** Error over 1-σ uncertainty for the set of geophysical parameters.

| Parameter | Error/1-σ Uncertainty |
|---|---|
| $GM$ | 1.8 |
| $\overline{J}_2$ | 2.6 |
| $\overline{C}_{22}$ | 2.0 |
| $k_{2r}$ | 1.1 |
| $k_{2i}$ | 1.2 |
| Spin axis $\alpha$ | 1.1 |
| Spin axis $\beta$ | 1.6 |
| Libration amplitude $\phi_0$ | 0.9 |
| Mercury angular velocity $\omega$ | 0.8 |

**Table 6.** 3-σ uncertainties for the set of geophysical parameters.

| Parameter | HgM008 [16] | MESS160A [30] | MORE |
|---|---|---|---|
| $\overline{J}_2$ | $1.1 \times 10^{-9}$ | $1.7 \times 10^{-8}$ | $1.3 \times 10^{-10}$ |
| $\overline{C}_{22}$ | $6.6 \times 10^{-10}$ | $2.4 \times 10^{-8}$ | $2.1 \times 10^{-10}$ |
| $k_{2r}$ | $2.5 \times 10^{-2}$ | $3.0 \times 10^{-2}$ | $1.3 \times 10^{-3}$ |
| $k_{2i}$ | / | / | $1.2 \times 10^{-3}$ |
| Spin axis $\alpha$ [arcsec] | 3.24 | 9.0 | $4.8 \times 10^{-1}$ |
| Spin axis $\beta$ [arcsec] | 1.08 | 6.1 | $3.6 \times 10^{-1}$ |
| Libration amplitude $\phi_0$ [arcsec] | 8.7 | / | $5.0 \times 10^{-1}$ |
| Mercury angular velocity $\omega$ [arcsec/day] | $4.7 \times 10^{-3}$ | $2.2 \times 10^{-2}$ | $2.0 \times 10^{-3}$ |
| Obliquity $\varepsilon$ [arcmin] | $2.7 \times 10^{-2}$ | $1.2 \times 10^{-1}$ | $5.5 \times 10^{-3}$ |

### *4.2. Rotation*

All the rotational parameter errors are inside the 3-$\sigma$ uncertainty, as can be seen in Table 5. Table 6 summarizes the expected accuracy in determining Mercury's rotational parameters. The right ascension and declination of the rotational pole can be estimated with uncertainties of 0.48 and 0.36 arcseconds, respectively. Accordingly, Mercury's obliquity can be determined at a level of $5.5 \times 10^{-3}$ arcmin. The libration amplitude in longitude is expected to be resolved to within 0.50 arcseconds, corresponding to a few meters at the equator. This enhanced accuracy could constrain the size of the solid inner core, if present, with respect to Mercury's liquid outer core [53]. The resulting uncertainty of $C/MR^2$ is $9.2 \times 10^{-4}$, while $C_m/C$ can be determined at the level of $5.9 \times 10^{-3}$, using Peale's procedure [17].

### *4.3. Positioning*

The positioning of the MPO in the Hermean frame is a crucial task to ensure reliable scientific results from the other instruments. Figure 10 shows the propagation of the MPO 3-

σ position uncertainty during the first year of the orbital phase. For each arc, the uncertainty is reported at the beginning, center and final epochs. Purple and red bars point out the superior solar conjunctions and perihelia periods, respectively. The radial positioning of the spacecraft is the best determined, due to the gravity acceleration which constrains the MPO position along the spacecraft–planet direction, enabling accuracies at the level of few centimeters when tracking from ground is available. The position in the along-track and transverse directions is determined more poorly, still with 3-σ accuracies at the level of ten meters. The error, calculated as the difference between the estimated trajectory and the "true" one, is inside the 3-σ uncertainty in 95% of the arcs, indicating a successful trajectory reconstruction process.

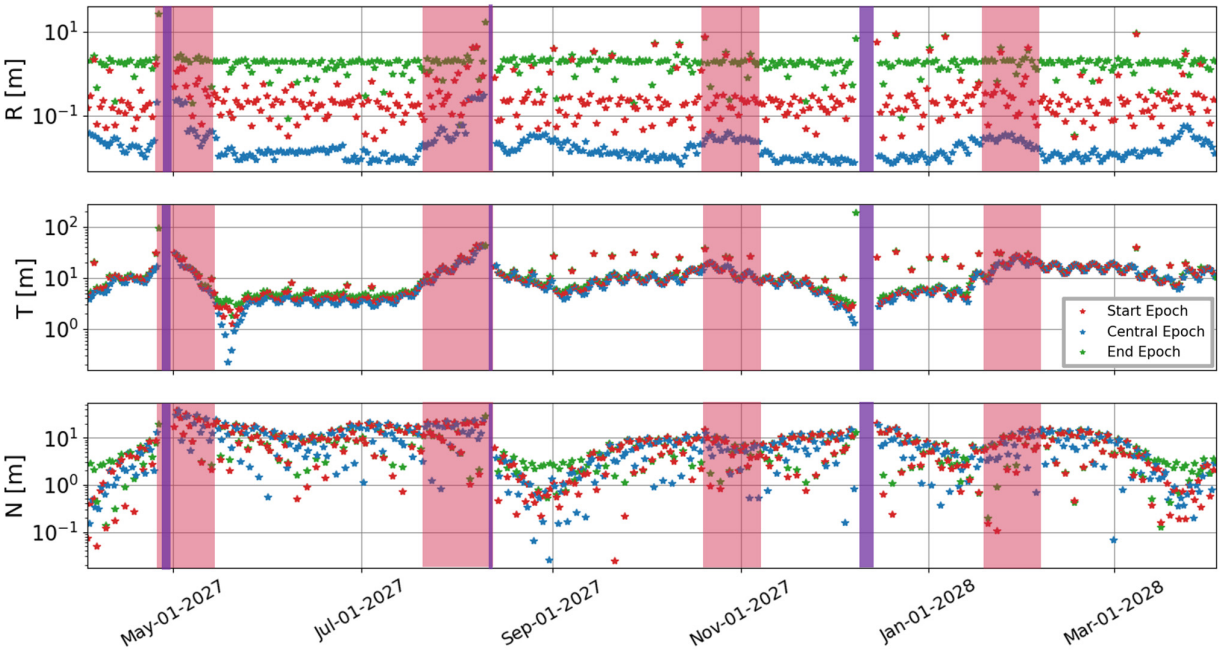



**Figure 10.** Position uncertainty components (3-$\sigma$) over the first year of the orbital phase. For each 24 h arc, the uncertainty is reported at the initial, central and final epoch. The central epoch of each arc is the closest to the tracking window, while the final epoch is where the inter-arc constraint is applied. Red and purple bars point out perihelia periods and intervals with impact parameters below $7R_{\odot}$, respectively.

Figure 11 shows the two-way range-rate post-fit residuals over the first 20 days of the orbital phase. The residuals exhibit no systematic signatures, and their RMS is consistent with the expected noise level of the Ka-band radio link (see Table 1), demonstrating a good fit for the observations.

Figure 12 shows the propagation of the MPO 3-σ position uncertainty during a 1-day observation arc, together with the times of the desaturation maneuvers execution, considering the nominal scenario with two maneuvers per day. The first maneuver, carried out in the tracking period, does not impact the spacecraft's positioning accuracy, since it can be estimated well by means of radio tracking data. The second maneuver, carried out when no tracking is available, is instead constrained only by imposing matching conditions among subsequent arcs through the inter-arc constraint. The constraint value of 0.73 mm/s for the matching of velocities among subsequent arcs imposes a lower bound for the absolute sensitivity of the second maneuver. The uncertainty in the radial components increases rapidly after the out-of-pass desaturation maneuver reaching values compatible with the threshold imposed by the inter-arc constraints (1 m).

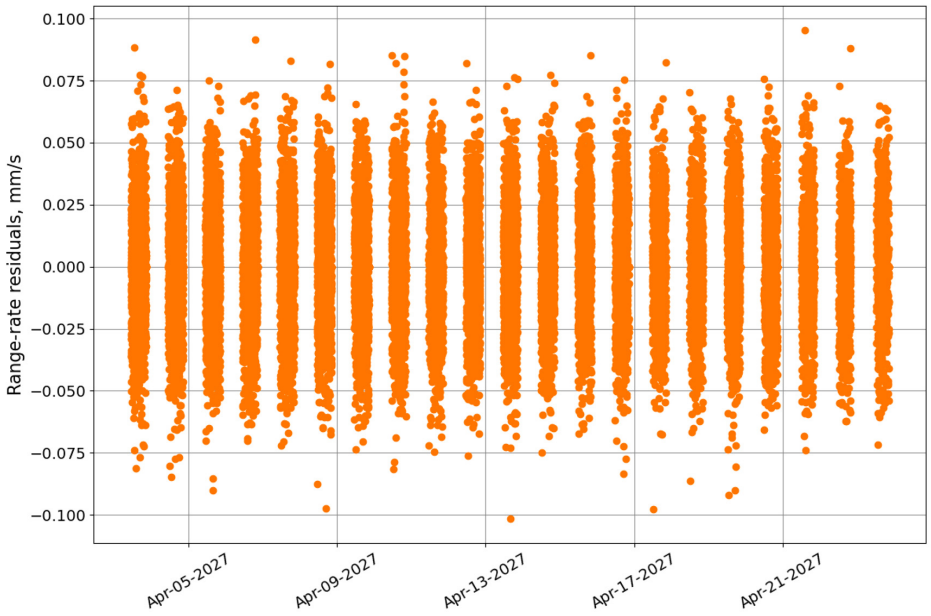



**Figure 11.** Two-way range-rate post-fit residuals over the first 20 days of the orbital phase.

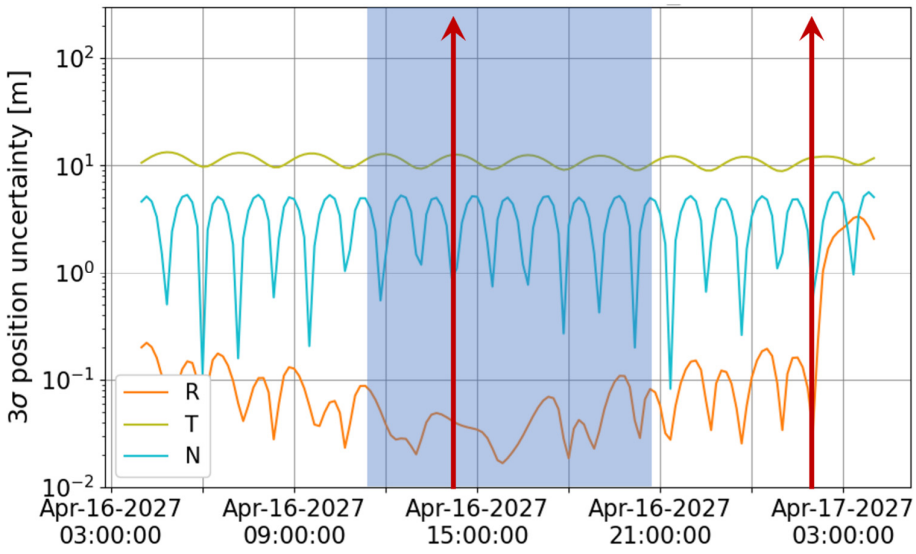



**Figure 12.** Position uncertainty (3-σ) for one arc (radial, transverse and normal components) with two daily maneuvers. The red arrows represent the wheel off-loading maneuvers. The blue block is the tracking pass.

An alternative contingency scenario involves the use of one maneuver every three orbits (three or four maneuvers per day). In this case, the occurrence of multiple maneuvers outside the tracking pass does not allow us to distinguish their individual contributions to the spacecraft dynamics through inter-arc constraints. The removal of inter-arc constraints has a minor impact on the geodesy experiment, leading to a degradation of 10–20% in the set of estimated parameters. On the other hand, it has a strong impact on the trajectory reconstruction performance. In the absence of such constraints, the positioning accuracy strongly degrades after the out-of-pass desaturation maneuvers, as shown in Figure 13, reaching tens of meters in the radial and normal direction and hundreds of meters in the transverse direction.

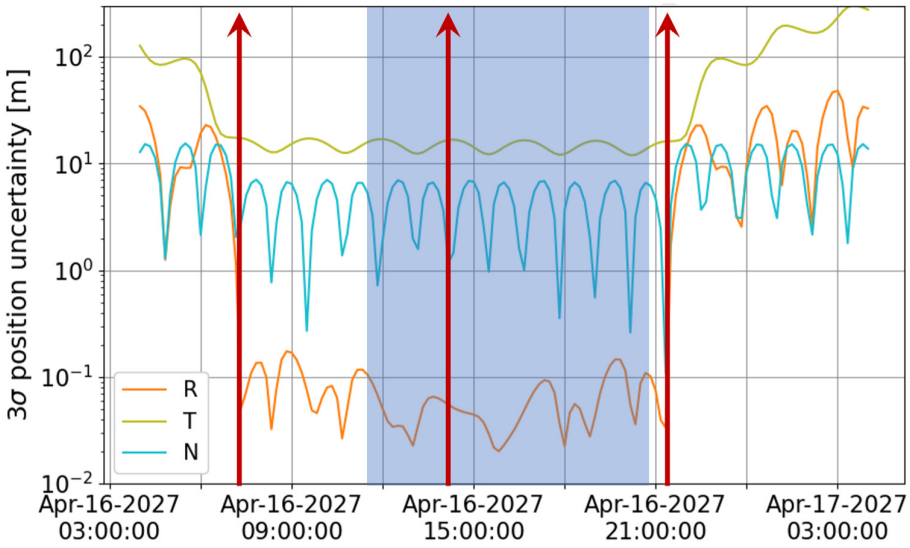



**Figure 13.** Position uncertainty (3-σ) for one arc (radial, transverse and normal components) with one maneuver every three orbits. The red arrows represent the wheel off-loading maneuvers. The blue block is the tracking pass.

## 5. Conclusions

In this work, we have analyzed the performance of the MORE gravity and rotation experiment of BepiColombo, taking into account the effect of inaccuracies in the force models. This analysis therefore represents a contingency scenario in which measurements of the ISA accelerometer will not be available. We account for errors in the spacecraft reference state and optical properties, unbalanced ΔVs due to wheel off-loading maneuvers, solar irradiance fluctuations, residual effects due to unmodeled non-gravitational accelerations and the not perfectly known gravity and rotation model. We solve for the set of geophysical parameters and the gravity field coefficients up to degree and order 70, constrained with a Kaula rule ($A_k$ = 10) for degrees greater than 30.

The analysis is subject to two main limitations: (i) the force models used for simulating the observables and for estimation share the same mathematical formulation and (ii) we do not account for sporadic unexpected accelerations. Under these assumptions and with the adopted perturbation levels, our results show that the OD filter effectively compensates for the introduced mismodeling without including ISA data. Future work may consider a mismatch in the physical and numerical models between the simulation of observables and estimation steps.

We provide updated accuracy estimates for the gravity and rotation experiment over the two-year orbital phase, using only Doppler data. The uncertainties derived from our analysis confirm that MORE is expected to provide a reliable, high-resolution gravity field in the southern hemisphere. This refined gravity field will enhance our understanding of the processes that shaped Mercury's surface, offering valuable insights into the planet's geological history. The estimation of the Love number $k_2$ can be improved at the level of $1.3 \times 10^{-3}$ (3-σ), allowing us to set tighter constraints on the interior structure of Mercury. The estimation of the pole's right ascension and declination can be estimated better than a half arcsecond. The amplitude of Mercury's physical librations in longitude can be determined with an accuracy of a few meters at the equator. Mercury's obliquity can be retrieved with an accuracy of ~$5.5 \times 10^{-3}$ arcmin, improving the determination of the dimensionless moment of inertia and the ratio between the principal moment of inertia of the mantle and that of the entire planet.

Furthermore, the precise radio tracking enables good accuracy in the spacecraft positioning. With two daily wheel off-loading maneuvers, the expected orbit reconstruction

accuracy is at the level of a few tens of centimeters in the radial direction, and a few meters in the normal and transverse directions (3-σ values). With an increment in maneuver frequency, this accuracy is expected to degrade to several tens of meters in the radial and normal directions, and to hundreds of meters in the transverse direction. While in the first case, the laser altimetric measurements can take full advantage of the spacecraft positioning in the Hermean frame, this is no longer true when the frequency of the desaturation events is increased. In this latter case, the altimetric measurements cannot be properly referenced for the Mercury geoid for quite a significant fraction of the orbital period.

**Author Contributions:** Conceptualization, A.Z., I.d.S., P.C., U.D.F., and L.I.; methodology, A.Z., I.d.S., and P.C.; software, A.Z., I.d.S., and P.C.; validation, A.Z.; formal analysis, A.Z.; investigation, A.Z.; resources, A.Z., I.d.S., P.C., and U.D.F.; data curation, A.Z.; writing—original draft preparation, A.Z.; writing—review and editing, A.Z., I.d.S., P.C., U.D.F., and L.I.; visualization, A.Z.; supervision, L.I.; project administration, L.I.; funding acquisition, L.I. All authors have read and agreed to the published version of the manuscript.

**Funding:** This research received no external funding.

**Data Availability Statement:** The raw data supporting the conclusions of this article will be made available by the authors on request.

**Acknowledgments:** This work was funded in part by the Italian Space Agency, under contract n. 2022-16-HH.1-2024.

**Conflicts of Interest:** Authors Paolo Cappuccio and Umberto De Filippis were employed by the company Aurora Technology for ESAC. The remaining authors declare that the research was conducted in the absence of any commercial or financial relationships that could be construed as a potential conflict of interest.

## Abbreviations

The following abbreviations are used in this manuscript:

| | |
|---|---|
| DSA | Deep Space Antenna |
| ESA | European Space Agency |
| HGA | High Gain Antenna |
| IAU | International Astronomical Union |
| IR | Infrared |
| ISA | Italian Spring Accelerometer |
| JAXA | Japan Aerospace Exploration Agency |
| KaT | Ka-band Transponder |
| MDIS | Mercury Dual Imaging System |
| MORE | Mercury Orbiter Radio-science Experiment |
| MTA | Mercury True Anomaly |
| OD | Orbit Determination |
| RTN | Radial, Transverse and Normal |
| SPE | Sun–Probe–Earth angle |
| SRP | Solar Radiation Pressure |
| SSC | Superior Solar Conjunction |
| TRP | Thermal Recoil Pressure |
| TSI | Total Solar Irradiance |
| WOL | Wheel Off-Loading |

## References


1. Giberson, W.E.; Cunningham, N.W. Mariner 10 mission to Venus and Mercury. *Acta Astronaut.* **1975**, *2*, 715–743. [CrossRef]
2. Solomon, S.C.; McNutt, R.L.; Gold, R.E.; Domingue, D.L. MESSENGER Mission Overview. In *The Messenger Mission to Mercury*; Springer: New York, NY, USA, 2007; pp. 3–39. [CrossRef]
3. Benkhoff, J.; Murakami, G.; Baumjohann, W.; Besse, S.; Bunce, E.; Casale, M.; Cremosese, G.; Glassmeier, K.-H.; Hayakawa, H.; Heyner, D.; et al. BepiColombo-Mission Overview and Science Goals. *Space Sci. Rev.* **2021**, *217*, 90. [CrossRef]
4. Mangano, V.; Dósa, M.; Fränz, M.; Milillo, A.; Oliveira, J.S.; Lee, Y.J.; McKenna-Lawlor, S.; Grassi, D.; Heyner, D.; Kozyrev, A.S.; et al. BepiColombo Science Investigations During Cruise and Flybys at the Earth, Venus and Mercury. *Space Sci. Rev.* **2021**, *217*, 23. [CrossRef]
5. Genova, A.; Hussmann, H.; Van Hoolst, T.; Heyner, D.; Iess, L.; Santoli, F.; Thomas, N.; Cappuccio, P.; di Stefano, I.; Kolhey, P.; et al. Geodesy, Geophysics and Fundamental Physics Investigations of the BepiColombo Mission. *Space Sci. Rev.* **2021**, *217*, 31. [CrossRef]
6. Iess, L.; Asmar, S.W.; Cappuccio, P.; Cascioli, G.; De Marchi, F.; di Stefano, I.; Genova, A.; Ashby, N.; Barriot, J.P.; Bender, P.; et al. Gravity, Geodesy and Fundamental Physics with BepiColombo's MORE Investigation. *Space Sci. Rev.* **2021**, *217*, 21. [CrossRef]
7. Imperi, L.; Iess, L. The determination of the post-Newtonian parameter $\gamma$ during the cruise phase of BepiColombo. *Class. Quantum Gravity* **2017**, *34*, 075002. [CrossRef]
8. Bertotti, B.; Comoretto, G.; Iess, L. Doppler tracking of spacecraft with multi-frequency links. *Astron. Astrophys.* **1993**, *269*, 608–616.
9. CCSDS. *Pseudo-Noise (PN) Ranging Systems*; Consultative Committee for Space Data Systems (CCSDS): Washington, DC, USA, 2014.
10. Imperi, L.; Iess, L.; Mariani, M.J. An analysis of the geodesy and relativity experiments of BepiColombo. *Icarus* **2018**, *301*, 9–25. [CrossRef]
11. De Marchi, F.; Cascioli, G. Testing general relativity in the solar system: Present and future perspectives. *Class. Quantum Gravity* **2020**, *37*, 095007. [CrossRef]
12. De Filippis, U.; Lefevre, C.; Lucente, M.; Magnafico, C.; Santoli, F.; Cappuccio, P.; di Stefano, I.; Zurria, A.; Iess, L. Pseudo-Drag-Free System Simulation for Bepicolombo Radio Science Using Accelerometer Data. *J. Guid. Control Dyn.* **2024**, *47*, 685–696. [CrossRef]
13. Santoli, F.; Fiorenza, E.; Lefevre, C.; Lucchesi, D.M.; Lucente, M.; Magnafico, C.; Morbidini, A.; Peron, R.; Iafolla, V. ISA, a High Sensitivity Accelerometer in the Interplanetary Space. *Space Sci. Rev.* **2020**, *216*, 145. [CrossRef]
14. De Filippis, U.; Lefevre, C.; Lucente, M.; Magnafico, C.; Santoli, F. Characterization of the outgassing event during BepiColombo second Venus flyby using Italian Spring Accelerometer data. *Acta Astronaut.* **2025**, *226*, 11–19. [CrossRef]
15. Magnafico, C.; De Filippis, U.; Santoli, F.; Lefevre, C.; Lucente, M.; Lucchesi, D.; Fiorenza, E.; Peron, R.; Iafolla, V. Italian Spring Accelerometer measurements of unexpected Non Gravitational Perturbation during BepiColombo second Venus swing-by. *Acta Astronaut.* **2025**, *232*, 14–22. [CrossRef]
16. Genova, A.; Goossens, S.; Mazarico, E.; Lemoine, F.G.; Neumann, G.A.; Kuang, W.; Sabaka, T.J.; Hauck, S.A.; Smith, D.E.; Solomon, S.C.; et al. Geodetic Evidence That Mercury Has A Solid Inner Core. *Geophys. Res. Lett.* **2019**, *46*, 3625–3633. [CrossRef]
17. Peale, S.J. Does Mercury have a molten core? *Nature* **1976**, *262*, 765–766. [CrossRef]
18. Peale, S.J. The free precession and libration of Mercury. *Icarus* **2005**, *178*, 4–18. [CrossRef]
19. Thor, R.N.; Kallenbach, R.; Christensen, U.R.; Stark, A.; Steinbrügge, G.; Di Ruscio, A.; Cappuccio, P.; Iess, L.; Hussmann, H.; Oberst, J. Prospects for measuring Mercury's tidal Love number h2 with the BepiColombo Laser Altimeter. *Astron. Astrophys.* **2020**, *633*, A85. [CrossRef]
20. Steinbrügge, G.; Padovan, S.; Hussmann, H.; Steinke, T.; Stark, A.; Oberst, J. Viscoelastic Tides of Mercury and the Determination of its Inner Core Size. *J. Geophys. Res. Planets* **2018**, *123*, 2760–2772. [CrossRef]
21. Van Hoolst, T.; Jacobs, C. Mercury's tides and interior structure. *J. Geophys. Res. Planets* **2003**, *108*. [CrossRef]
22. Padovan, S.; Margot, J.; Hauck, S.A.; Moore, W.B.; Solomon, S.C. The tides of Mercury and possible implications for its interior structure. *J. Geophys. Res. Planets* **2014**, *119*, 850–866. [CrossRef]
23. Wieczorek, M.A.; Phillips, R.J. Potential anomalies on a sphere: Applications to the thickness of the lunar crust. *J. Geophys. Res. Planets* **1998**, *103*, 1715–1724. [CrossRef]
24. Tosi, N.; Grott, M.; Plesa, A.-C.; Breuer, D. Thermochemical evolution of Mercury's interior. *J. Geophys. Res. Planets* **2013**, *118*, 2474–2487. [CrossRef]
25. Smith, D.E.; Zuber, M.T.; Phillips, R.J.; Solomon, S.C.; Hauck, S.A.; Lemoine, F.G.; Mazarico, E.; Neumann, G.A.; Peale, S.J.; Margot, J.-L.; et al. Gravity Field and Internal Structure of Mercury from MESSENGER. *Science (1979)* **2012**, *336*, 214–217. [CrossRef]
26. Mazarico, E.; Genova, A.; Goossens, S.; Lemoine, F.G.; Neumann, G.A.; Zuber, M.T.; Smith, D.E.; Solomon, S.C. The gravity field, orientation, and ephemeris of Mercury from MESSENGER observations after three years in orbit. *J. Geophys. Res. Planets* **2014**, *119*, 2417–2436. [CrossRef]

27. Verma, A.K.; Margot, J. Mercury's gravity, tides, and spin from MESSENGER radio science data. *J. Geophys. Res. Planets* **2016**, *121*, 1627–1640. [CrossRef]
28. Kaula, W.M. *Theory of Satellite Geodesy: Applications of Satellites to Geodesy*; Blaisdell Publishing Company: Waltham, MA, USA, 1966.
29. Mazarico, E.; Genova, A.; Goossens, S.; Lemoine, F.G. The gravity field of Mercury from MESSENGER. In Proceedings of the Lunar and Planetary Institute Science Conference Abstracts, The Woodlands, TX, USA, 21–25 March 2016.
30. Konopliv, A.S.; Park, R.S.; Ermakov, A.I. The Mercury gravity field, orientation, love number, and ephemeris from the MESSENGER radiometric tracking data. *Icarus* **2020**, *335*, 113386. [CrossRef]
31. Genova, A.; Goossens, S.; Del Vecchio, E.; Petricca, F.; Beuthe, M.; Wieczorek, M.; Chiarolanza, G.; di Achille, G.; Mitri, G.; Di Stefano, I.; et al. Regional variations of Mercury's crustal density and porosity from MESSENGER gravity data. *Icarus* **2023**, *391*, 115332. [CrossRef]
32. Genova, A.; Iess, L.; Marabucci, M. Mercury's gravity field from the first six months of MESSENGER data. *Planet. Space Sci.* **2013**, *81*, 55–64. [CrossRef]
33. Tapley, B.D.; Schutz, B.E.; Born, G.H. *Statistical Orbit Determination*; Elsevier: Amsterdam, The Netherlands, 2004. [CrossRef]
34. Evans, S.; Taber, W.; Drain, T.; Smith, J.; Wu, H.-C.; Guevara, M.; Sunseri, R.; Evans, J. MONTE: The next generation of mission design and navigation software. *CEAS Space J.* **2018**, *10*, 79–86. [CrossRef]
35. Milani, A.; Gronchi, G. *Theory of Orbit Determination*, 1st ed.; Cambridge University Press: Cambridge, UK, 2010.
36. Milani, A.; Carpino, M.; Rossi, A.; Catastini, G.; Usai, S. Local geodesy by satellite laser ranging: A European solution. *Manuscripta Geod.* **1995**, *20*, 123–138. [CrossRef]
37. Thornton, C.L.; Border, J.S. *Radiometric Tracking Techniques for Deep-Space Navigation*; John Wiley & Sons, Inc.: Hoboken, NJ, USA, 2000.
38. Cappuccio, P.; Notaro, V.; di Ruscio, A.; Iess, L.; Genova, A.; Durante, D.; di Stefano, I.; Asmar, S.W.; Ciarcia, S.; Simone, L. Report on First Inflight Data of BepiColombo's Mercury Orbiter Radio Science Experiment. *IEEE Trans. Aerosp. Electron. Syst.* **2020**, *56*, 4984–4988. [CrossRef]
39. Di Stefano, I.; Iess, L.; Benedetto, C.; Di Achille, G.; Genova, A.; Mitri, G.; Negri, B.; Tommei, G.; Zannoni, M. The Mercury Orbiter Radioscience Experiment of the BepiColombo Mission. In *IAF Space Exploration Symposium*; International Astronautical Federation (IAF): Paris, France, 2024; pp. 853–866. [CrossRef]
40. Doria, I.; Cappuccio, P.; Durante, D.; di Stefano, I.; Bernacchia, D.; Manghi, R.L.; Zannoni, M.; Iess, L. Comparison of Plasma Calibration Techniques to Enhance Radiometric Observables Performance: BepiColombo MORE Test Case. *Radio Sci.* **2025**, *60*, e2025RS008441. [CrossRef]
41. Archinal, B.A.; Acton, C.H.; A'hearn, M.F.; Conrad, A.; Consolmagno, G.J.; Duxbury, T.; Hestroffer, D.; Hilton, J.L.; Kirk, R.L.; Klioner, S.A.; et al. Report of the IAU Working Group on Cartographic Coordinates and Rotational Elements: 2015. *Celest. Mech. Dyn. Astron.* **2018**, *130*, 22. [CrossRef]
42. Hawkins, S.E.; Boldt, J.D.; Darlington, E.H.; Espiritu, R.; Gold, R.E.; Gotwols, B.; Grey, M.P.; Hash, C.D.; Hayes, J.R.; Jaskulek, S.E.; et al. The Mercury Dual Imaging System on the MESSENGER Spacecraft. *Space Sci. Rev.* **2007**, *131*, 247–338. [CrossRef]
43. Kato, T.; van der Ha, J.C. Precise modelling of solar and thermal accelerations on Rosetta. *Acta Astronaut.* **2012**, *72*, 165–177. [CrossRef]
44. Wieczorek, M.A.; Meschede, M. SHTools: Tools for Working with Spherical Harmonics. *Geochem. Geophys. Geosystems* **2018**, *19*, 2574–2592. [CrossRef]
45. Kato, T.; Rievers, B.; Van der Ha, J.C.; Laemmerzahl, C. Sensitivity Analysis of the Non-Gravitational Perturbations on a Mercury Orbiter. *Adv. Astronaut. Sci.* **2012**, *143*, 1579–1595.
46. di Stefano, I.; Cappuccio, P.; Iess, L. Precise Modeling of Non-Gravitational Accelerations of the Spacecraft BepiColombo During Cruise Phase. *J. Spacecr. Rocket.* **2023**, *60*, 1625–1638. [CrossRef]
47. Iafolla, V.; Lucchesi, D.-M.; Nozzoli, S.; Santoli, F. The BepiColombo mission to Mercury: Reaction wheels desaturation manoeuvres and the ISA accelerometer $\Delta V$ measurements. *Planet. Space Sci.* **2011**, *59*, 51–62. [CrossRef]
48. Kopp, G. Magnitudes and timescales of total solar irradiance variability. *J. Space Weather Space Clim.* **2016**, *6*, A30. [CrossRef]
49. Kopp, G.; Lawrence, G.; Rottman, G. Total irradiance monitor design and on-orbit functionality. In *Proceedings of the SPIE Optics + Photonics, San Diego, CA, USA, 4 February 2004*; Fineschi, S., Gummin, M.A., Eds.; SPIE: Bellingham, WA, USA, 2004; p. 14. [CrossRef]
50. Margot, J.; Peale, S.J.; Solomon, S.C.; Hauck, S.A.; Ghigo, F.D.; Jurgens, R.F.; Yseboodt, M.; Giorgini, J.D.; Padovan, S.; Campbell, D.B. Mercury's moment of inertia from spin and gravity data. *J. Geophys. Res. Planets* **2012**, *117*. [CrossRef]
51. Folkner, W.M.; Williams, J.G.; Boggs, D.H.; Park, R.S.; Kuchynka, P. The Planetary and Lunar Ephemerides DE430 and DE431. *Interplanet. Netw. Prog. Rep.* **2014**, *196*, 42–196.

52. Konopliv, A.S.; Asmar, S.W.; Bills, B.G.; Mastrodemos, N.; Park, R.S.; Raymond, C.A.; Smith, D.E.; Zuber, M.T. The Dawn Gravity Investigation at Vesta and Ceres. *Space Sci. Rev.* **2011**, *163*, 461–486. [CrossRef]
53. Van Hoolst, T.; Rivoldini, A.; Baland, R.-M.; Yseboodt, M. The effect of tides and an inner core on the forced longitudinal libration of Mercury. *Earth Planet. Sci. Lett.* **2012**, *333–334*, 83–90. [CrossRef]

**Disclaimer/Publisher's Note:** The statements, opinions and data contained in all publications are solely those of the individual author(s) and contributor(s) and not of MDPI and/or the editor(s). MDPI and/or the editor(s) disclaim responsibility for any injury to people or property resulting from any ideas, methods, instructions or products referred to in the content.